

High-Energy Fragmentation in Nanophotonic Ion Production by Laser-Induced Silicon Microcolumn Arrays[†]

Jessica A. Stolee, Yong Chen,[‡] and Akos Vertes*

Department of Chemistry, George Washington University, Washington, D.C. 20052

Received: July 19, 2009; Revised Manuscript Received: September 9, 2009

Laser-induced silicon microcolumn arrays (LISMA) exhibit nanophotonic ion production in laser desorption ionization experiments (Walker et al., *Angew. Chem., Int. Ed.* **2009**, *48*, 1669) for small-to-medium-size molecules. Although these surfaces are known to promote fragmentation of adsorbates at high laser fluences, the nature, extent, and origin of peptide ion decomposition remains unknown. Here we demonstrate that peptide ions, e.g., bradykinin, leucine enkephalin, angiotensin I, substance P, and various tripeptides, desorbed from these substrates show an increasing degree of fragmentation as the fluence is raised. Compared to other ion fragmentation methods, LISMA shows similarity to high-energy collision activated dissociation (CAD), ion decomposition produced by metastable atom beams, and surface induced dissociation (SID). While some of the produced fragments are associated with high-energy decomposition channels, for example, the abundant *a*₅ fragment produced from singly protonated bradykinin ion, other ions in the same spectra (e.g., the ammonia loss from the protonated bradykinin ion) are predominantly produced by low energy processes. To explore the role of internal energy in the fragmentation of ions produced from LISMA, the survival yields of eight benzyl-substituted benzylpyridinium thermometer ions were also studied as a function of laser fluence and surface derivatization. The corresponding internal energies were determined using the Rice–Ramsperger–Kassel–Marcus formalism. On both native and silane-derivatized surfaces, the thermometer ions showed stable internal energy values over a wide range of laser fluences. This presented a strong contrast to the behavior of the peptides that yielded high-energy fragments at increased fluence. As the thermometer ions did not record an increase in internal energy, the enhanced fragmentation of the peptides was indicative of alternative high-energy mechanisms.

Introduction

Micro- and nanostructured silicon surfaces can be produced by femtosecond and nanosecond laser irradiation.^{1,2} Repeated exposure of a silicon wafer to picosecond laser pulses creates two-dimensional arrays of protrusions called laser-induced silicon microcolumn arrays (LISMA) that serve as efficient platforms for soft laser desorption ionization.³ These mesostructured surfaces, also termed black silicon, possess uniformly high absorptivity in a broad wavelength range (from 200 nm to the mid-IR).

In laser desorption ionization experiments, LISMA exhibit highly polarization dependent ion production.⁴ This behavior is explained in terms of nanophotonic interactions that show similarities to the behavior of optical antenna arrays. The ionization mechanism on these structures and their ability to induce peptide fragmentation at elevated fluences remains unexplained.

Near-field fluorescence measurements in the vicinity of nanoscopic protrusions on silicon indicate a strong enhancement of the electric field, *E*, at a distance, *r*, from the origin:⁵

$$\mathbf{E} = -\kappa|\mathbf{E}_L|\left(\frac{a}{r}\right)^3 \mathbf{r} \quad (1)$$

where \mathbf{E}_L is the electric field vector of the laser radiation, *a* is the radius of curvature of the protrusion, and \mathbf{r} is a unit vector pointing

away from the protrusion. The enhancement factor, κ , for a 3:1 aspect ratio protrusion is ~ 6 , which translates into a laser irradiance enhancement of ~ 36 .⁵ Thus, the adsorbed molecules and the desorbed ions in the vicinity of the microcolumns experience very strong fields and radiation intensities. These conditions can contribute to the ionization and, through ion activation, to the fragmentation processes.

Other soft ionization sources, such as matrix-assisted laser desorption ionization (MALDI) produce low-internal-energy peptide ions with minimum amount of fragmentation.^{6–8} The need for complementary soft ionization methods, capable of small molecule analysis, has led to the introduction of nano-materials and nanostructures that facilitate desorption and ionization without using a matrix. Recently, desorption ionization on silicon (DIOS) based on a nanoporous silicon substrate⁹ and nanostructure-initiator mass spectrometry (NIMS)¹⁰ were introduced as versatile laser desorption ionization substrates. Fragmentation of preformed ions on DIOS showed reduced sensitivity to laser fluence changes.¹¹

Peptide ions produced by these ionization platforms remain intact in the source region of the mass spectrometer. To induce their fragmentation, an additional activation step is required. These include collision activated dissociation (CAD),^{12,13} black-body infrared radiative dissociation (BIRD),¹⁴ surface induced dissociation (SID),^{15–17} electron capture dissociation (ECD),^{18,19} electron transfer dissociation (ETD),²⁰ and ion decomposition produced by metastable atom beams.^{21–23} Fragmentation of model peptides, e.g., bradykinin, leucine enkephalin, angiotensin I, and substance P, have been extensively studied by all of these methods.

[†] Part of the “Barbara J. Garrison Festschrift”.

* To whom correspondence should be addressed. Phone: (202) 994-2717. Fax: (202) 994-5873. E-mail: vertes@gwu.edu.

[‡] Current address: Genomics Institute of the Novartis Research Foundation, 10675 John Jay Hopkins Drive, San Diego, CA 92121.

Thermometer ions (TI), such as benzyl-substituted benzylpyridinium cations, are preformed ions with a single decomposition channel that, in a laser desorption ionization experiment, can report on internal energy transfer in the desorption step separately from the energy gain due to ionization.^{24,25} The survival yield method based on TI has been utilized to gauge the internal energy of ions generated by electrospray ionization,^{26–32} MALDI,^{6,7,33–36} DIOS,^{11,37} desorption electrospray ionization,³⁸ and silicon nanowires (SiNW).³⁹

Other methods developed for internal energy measurements include the deconvolution method that correlates the internal energy distribution, $P(E)$, to the decomposition spectrum and the breakdown curve.⁴⁰ According to the thermometer ion method, $P(E)$ can be estimated from the ion abundances measured in unimolecular decomposition with known thermochemical parameters.^{41,42} A modified version of the thermometer ion method, the above-mentioned survival yield method, is based on the correlation between the survival yield, SY,

$$SY = \frac{I(M^+)}{I(F^+) + I(M^+)} \quad (2)$$

where $I(M^+)$ and $I(F^+)$ are the abundances of the molecular ion and fragment ion, respectively, and the critical energy of the molecular ion.⁴³

Nanophotonic ion production from LISMA structures shows structure-specific peptide fragmentation at high laser fluences.³ This sets LISMA apart from MALDI and many other soft ionization techniques. The polarization and incidence angle dependence of energy deposition into LISMA structures was explained by axial currents in the microcolumns induced by the electromagnetic radiation of the desorption laser.⁴ The related energy dissipation is similar to Ohmic losses in antenna arrays. Biomolecular adsorbates on the microcolumns are rapidly desorbed from the heated surface. Desorption of the TI results in the direct production of ions, whereas most peptides require an additional ionization step. This difference enables us to discern if the origin of peptide fragmentation is linked to the internal energy gained during desorption.

The desorbed components in the plume can be ionized and activated through homogeneous and surface reactions. These processes include photoionization due to the local electric field, interactions with the hydroxy-terminated sites on the silicon microcolumns, proton transfer from solvent residues, and reactions with the electrons emitted from the silicon surface.^{9,44} At high laser intensities hydrogen-free radicals may form, due to the interaction of the elevated electron density with protons from the solvent residues, potentially causing in-source decay and peptide fragmentation.^{3,45} As it is shown in eq 1, the microcolumns can also induce local enhancements in the electromagnetic field that might also promote fragmentation.

In this contribution, we survey the type and abundance of fragments produced from peptide ions generated on LISMA substrates by laser radiation at increased fluence levels. By comparing the fragmentation of model peptides in LISMA ion production to results with low- and high-energy ion activation methods, we can discern the nature of the processes involved. We also probe the energy content of TI generated from LISMA and compare it to fragmentation patterns for peptides. The fluence dependence of fragmentation from these two types of adsorbates reveals the relationship between peptide fragmentation and internal energy effects on these nanophotonic structures. Studying the energy transfer into the preformed TI from LISMA

gives insight into the desorption process and enables comparisons with other soft laser desorption ionization methods. Chemical surface modifications are used to alter the interaction energy between the ions and the LISMA surface, and the resulting changes in the efficiency of energy transfer are evaluated.

Materials and Methods

Materials and Sample Preparation. Low-resistivity (~ 0.001 – $0.005 \text{ } \Omega \cdot \text{cm}$) p-type silicon wafers were purchased from University Wafer (South Boston, MA). Deionized water ($18.2 \text{ M}\Omega \cdot \text{cm}$) was produced with an E-pure system (Barnstead, Dubuque, IA), whereas reagent grade methanol was obtained from Sigma. Bradykinin (Arg-Pro-Pro-Gly-Ser-Phe-Pro-Phe-Arg), leucine enkephalin (Tyr-Gly-Gly-Phe-Leu), angiotensin I (Asp-Arg-Val-Tyr-Ile-His-Pro-Phe-His-Leu), substance P (Arg-Pro-Lys-Pro-Gln-Gln-Phe-Phe-Gly-Leu-Met-NH₂), and tripeptides Gly-Phe-Ser and Tyr-Gly-Gly were purchased from Sigma and used without further purification. Gly-Phe-Leu was purchased from Synbiosci (Livermore, CA). Chloride salts of eight benzyl-substituted benzylpyridinium ions (with 4-nitro- (4N), 4-chloro- (4C), 4-fluoro- (4F), 4-methoxy- (4MO), 3-methoxy- (3MO), 4-methyl- (4M), 3-methyl- (3M), and 2-methyl- (2M) substituents) were custom synthesized by Celestial Specialty Chemicals (Nepean, Ontario, Canada) and $1.0 \times 10^{-5} \text{ M}$ solutions were prepared daily in 50% methanol. For laser desorption ionization experiments $1.0 \text{ } \mu\text{L}$ of these solutions was deposited on LISMA substrates and dried under ambient conditions.

Synthesis of LISMA and Surface Derivatization. A detailed description of LISMA production can be found elsewhere.³ Briefly, the silicon wafers were cleaved into chips of 9 mm^2 surface area, cleaned with methanol and deionized water, air-dried, attached to the bottom of a Petri dish with double-sided tape, and submerged in 5 mL of deionized water at a depth of $\sim 2.6 \text{ mm}$. Microcolumns were generated by irradiating the silicon chips with 600 laser shots of 22 ps length from a frequency tripled Nd:YAG laser (PL2143, EKSPLA, Vilnius, Lithuania) at 0.13 J/cm^2 fluence. For surface characterization of the laser processed spot, a JEOL JSM-840A (Peabody, MA) scanning electron microscope (SEM) and a Hitachi FE-SEM S-4700 (Hitachi, Pleasanton, CA) were used.

For derivatization, the LISMA surfaces were oxidized with ozone, placed in a Petri dish, and covered with $15 \text{ } \mu\text{L}$ of (pentafluorophenyl)propyldimethylchlorosilane (PFPPDCS) (Gelest, Inc., Morrisville, PA). Subsequently, they were baked in an oven for 30 min to create a perfluorophenyl (PFP)-derivatized LISMA surface. The derivatized LISMAs were rinsed thoroughly with methanol and deionized water and air-dried.

Instrumentation and Data Acquisition. For the peptide fragmentation experiments, a high-resolution reflectron time-of-flight mass spectrometer (Axima CFR, Shimadzu-Kratos, Manchester, UK) was used. A home-built linear time-of-flight mass spectrometer (TOF-MS) with delayed extraction and a 4 ns pulse length nitrogen laser was used for the thermometer ion and survival yield experiments. The detailed description of the instrument can be found elsewhere.⁴⁶ The laser fluence was adjusted by a variable attenuator (935-5-OPT, Newport, Fountain Valley, CA) and calculated from the laser focal area and pulse energy, measured by a burn mark on photographic paper, and with a pyroelectric joule meter (model J4-05, Moletron, Portland, OR), respectively.

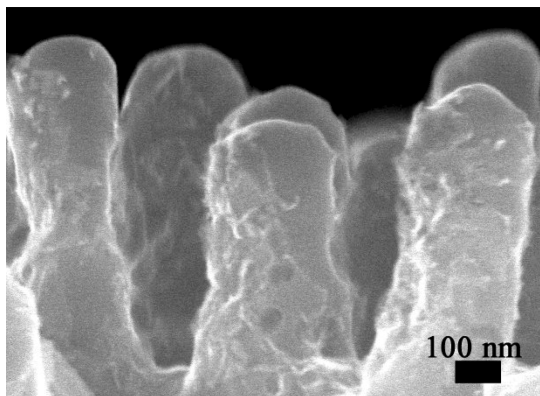


Figure 1. Side view of silicon microcolumns in a LISMA structure captured by SEM confirms that the column dimensions are commensurate with the laser wavelength.

For each sample, 20 spectra were taken at 10 different locations on the LISMA for a total of 200 spectra. Peak areas of molecular and fragment ions were then integrated and used to calculate experimental survival yields. The survival yields were converted into experimental rate coefficients, k_{exp} ,

$$k_{\text{exp}} = - \left(\frac{1}{\tau} \right) \ln(\text{SY}) \quad (3)$$

where τ , the reaction time in the acceleration region, is estimated as 100 ns for all TI.⁶

Rate Coefficient Calculations. The vibrational frequencies for the TI were previously calculated using AM1 semiempirical molecular orbital calculations with PC Spartan version 1.3 (Wave function, Irvine, CA),⁶ and the critical energy values of the TI were obtained from the literature.^{24,26} The unimolecular decomposition rate coefficient, $k(E)$, for a particular energy, E , can be calculated with the Rice–Ramsperger–Kassel–Marcus (RRKM) theory,

$$k(E) = \frac{G^*(E - E_0)}{hN(E)} \quad (4)$$

Where E_0 is the critical energy, $G^*(E - E_0)$ is the number of states between E and E_0 in the transition state, and $N(E)$ is the density of quantum states at energy E .⁴⁷ The computer program MassKinetics Scientific, Version 1.9, was used for the RRKM calculations.⁴⁸

Results and Discussion

LISMA Morphology. SEM imaging before and after laser irradiation confirmed that during the ion production experiments the microcolumns remained intact. Figure 1 shows a few columns from a typical LISMA structure used in this study. Measurements on the SEM images indicated an average diameter, periodicity and height of 400, 600, and 800 nm, respectively. Thus, the aspect ratio of the microcolumns was 2:1, which at the column surface resulted in a field enhancement factor of $\kappa \approx 4$ and an enhancement of the laser irradiance of ~ 16 . According to eq 1, moving away from the surface the enhanced field decays as $(ar)^3$, where the microcolumn tip radius of curvature, $a = \sim 200$ nm.

The dimensions of the LISMA are commensurate with the 337 nm wavelength of the desorption laser. On the basis of the polarization and incidence angle dependence of the ion yield

demonstrated earlier,⁴ these columns are heated by the axial current induced in them by the parallel component of the electric field in the laser radiation. From the SEM images, it is also evident that the individual microcolumns exhibit coarse textural features that increase the surface area.

LISMA Spectra of TI and Peptides. Mass spectra of all the TI desorbed from native and PFP-derivatized LISMA were obtained for a range of laser fluences. The fluence threshold for detectable ion production was ~ 26 mJ/cm² that exhibited slight variations. The molecular ion peak, M^+ , and a single fragment peak due to pyridine loss, F^+ , were observed, indicating that the energy deposited into the TI at the threshold fluence was at or above the critical energy of the fragmentation channel. The spectral identifications were straightforward as no external interferences, such as silicon clusters or alkaline adducts, were detected even at high fluences. Relative peak intensities in the TI spectra remained largely unchanged throughout the studied fluence range between 26 and 44 mJ/cm².

Bradykinin spectra at low fluences showed predominantly the quasi-molecular ion peaks (protonated and sodiated) (see the black trace in Figure 2A). As the fluence was raised, an increasing number and abundance of structure specific fragments were observed (see the wine, olive, and blue traces in Figure 2A). At the highest fluence level, we detected the $[M - \text{NH}_3 + \text{H}]^+$, y_8 , y_7 , a_5 , a_6 , d_{a6} , and c_5 ions as major fragments, and c_8 , Y_8 , a_8 , Y_7 , w_{a7} , a_7 , y_6 , y_5 , and v_5 as minor breakdown products (see Figure 2B).

Extensive fragmentation was observed for other peptides, such as leucine enkephalin (see Table 2 for the list of fragments and their intensities), angiotensin I, substance P, and tripeptides Gly-Phe-Ser, Gly-Phe-Leu, and Tyr-Gly-Gly. In regular MALDI experiments without collisional activation, none of these peptides exhibited fragmentation. The fluence-dependent fragmentation of bradykinin and the other small peptides was in sharp contrast to the TI fragmentation that remained unchanged in a wide fluence range.

The bradykinin fragments produced by LISMA at high laser fluences show major deviations from the species generated by low-energy CAD¹² or by BIRD¹⁴ activation of the singly protonated molecule. Table 1 compares the fragments produced by some of the known activation methods. The fragmentation spectra on LISMA is clearly different from low-energy CAD and BIRD, and the electron capture dissociation (ECD) of the doubly protonated bradykinin.^{18,19} There are, however, remarkable similarities to the spectra produced by high-energy CAD,¹³ metastable atom beams,^{21,22} and surface induced dissociation (SID) at 50 eV primary ion energy.¹⁵ Of these three latter techniques, metastable helium atoms, He(2¹S) and He(2³S), generate abundant a_5 and c_5 species that are also prevalent in the LISMA spectra. The excitation energies of the He(2¹S) and He(2³S) metastables are 20.6 and 19.8 eV, respectively. Inspecting the high-energy CAD and the LISMA spectra reveals that both contain major peaks for the a_5 , a_6 , and y_7 ions with kinetic energy losses of 22.9, 19.7, and 11.1 eV, respectively, in the CAD experiment.¹³ The correlation between the LISMA and the SID ions is the strongest. In the $520 < m/z < 910$ range all of the significant ions reported by the two methods are the same. The similarity in fragmentation between the three high-energy techniques and LISMA means that the production of most fragments in LISMA is likely a high-energy process.

In contrast to these three high-energy techniques, however, the LISMA spectra contain significant amounts of $[M - \text{NH}_3 + \text{H}]^+$ ions characteristic of low-energy CAD and BIRD spectra.

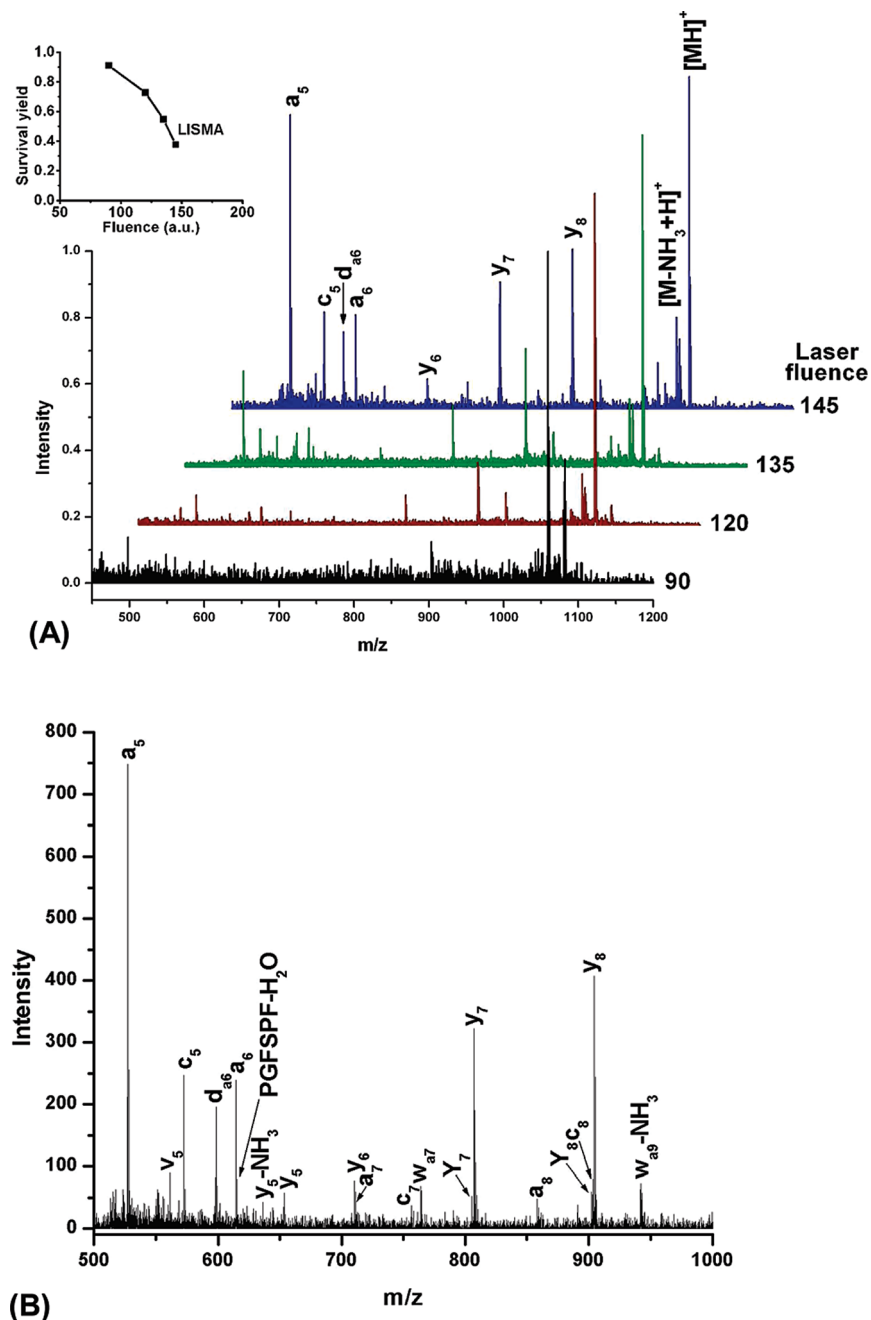


Figure 2. Peptide ion fragmentation in laser desorption from LISMA structures. (A) Bradykinin shows increasing variety and abundance of fragments as the laser fluence is increased. The molecular ion survival yield falls rapidly (see inset). (B) Enlarged segment of the high laser fluence (145 arbitrary units) spectrum in the $500 < m/z < 1000$ range that shows the assignment of all the major and minor fragments.

The presence of this fragment suggests that, in addition to the high-energy processes responsible for the *a*-series and internal fragment ions, a low-energy mechanism is also operational. To our knowledge, there is no ion activation method available that can access low- and high-energy fragments in the same experiment.

The LISMA spectra of leucine enkephalin also revealed the presence of fragments associated with high-energy processes. Table 2 lists the observed fragments and their abundances. The formation of the highly abundant b_3 and the *Y* and *F* immonium ions require relatively higher energy than the b_4 and a_4 fragments that are present with low to medium abundance. The energetics of the various fragmentation channels is revealed by threshold energies¹⁶ measured in SID and kinetic energy loss data¹³ for high-energy CAD in Table 2.

Similarities between the leucine enkephalin fragmentation patterns in LISMA and SID spectra recorded at 50 eV primary ion energy were especially pronounced. Comparable correlation was observed for the fragments of protonated angiotensin I. At elevated laser fluence, LISMA produced over 20 structure specific fragments from this ion, half of which were also found in the 100 eV SID spectra of the angiotensin I.¹⁷ The similarities between LISMA and SID spectra raise the possibility of a mechanistic relationship between the two techniques. The energetic ions produced in the troughs of the LISMA structure can collide with the microcolumn surfaces before being extracted into the mass spectrometer.

Survival Yields in LISMA Ion Production. To explore the significance of internal energy transfer in LISMA, the survival yield method was applied to a set of TI. Survival yields were

TABLE 1: Comparison of Protonated Bradykinin Fragmentation Patterns for LISMA at High Fluence with Various Methods of Ion Activation^a

activation method	conditions	major fragments	kinetic energy loss in CAD (eV) ^e	energy (eV)	minor fragments
LISMA at high fluence		[M - NH ₃ + H] ⁺ , y ₈ , y ₇ , a ₅ , a ₆ , d _{a6} , c ₅			c ₈ , Y ₈ , a ₈ , Y ₇ , w _{a7} , a ₇ , y ₆ , y ₅ , v ₅
CAD at low energy ^b	213 °C, 20 s	[M - NH ₃ + H] ⁺		1.3	y ₇ , y ₆ , y ₅ , b ₈ , b ₂
BIRD ^c	191 °C, 45 s	[M - NH ₃ + H] ⁺		1.3	
ECD ^d for [M+2H] ²⁺		c ₅			c ₄ , c ₇ , c ₈ , a ₈ , z ₆ , z ₅
CAD at high energy ^e	energy loss measured	a ₅	22.9		
		a ₆	19.7		
		a ₈	15.1		
		b ₆	12.8		
		b ₈	17.8		
		y ₇	11.1		
		b ₈ + OH	5.6		
metastable atoms ^f	He(2 ¹ S) He(2 ³ S)	a ₃ , a ₅ , a ₄ , c ₅ , x ₆		~20	
SID ^g	50 eV	y ₈ , a ₅			a ₆ , y ₅ , a ₇ , w _{a7} , y ₇ , a ₈

^a The primary ion is singly charged unless noted otherwise. ^b Low-energy CAD data from McLuckey and co-workers.¹² ^c BIRD data from Williams and co-workers.¹⁴ ^d ECD data from Barran and co-workers,¹⁹ and Smith and co-workers.¹⁸ ^e Kinetic energy loss data from Glish and co-workers.¹³ ^f Metastable atom beam data from Berkout²¹ and Doroshenko.²² ^g SID data from Wysocki and co-workers.¹⁵

TABLE 2: Protonated Leucine Enkephalin Fragmentation for LISMA, High-Energy CAD and SID

fragment	LISMA abundance	kinetic energy loss in CAD (eV) ^a	threshold energy in SID (eV) ^b
L	high		
F	high		1.62
Y ₁	medium		
Y	high		1.42
GF-28	low		
a ₂	low		
GF	low		1.5
b ₂	medium		1.42
GGF-28	low		
GGF	low		1.5
b ₃	high	7.4	1.42
y ₂	low	4.4	1.37
y ₃	absent	3.6	1.37
a ₄	low/medium	5.7	1.3
b ₄	low	3.5	1.14
MH ⁺	medium		

^a Kinetic energy loss data from Glish and co-workers.¹³ ^b SID threshold energy data from Laskin.¹⁶

calculated using eq 2 for laser fluences ranging from 26 to 44 mJ/cm². The survival yield values correlated with the critical energy of the TI, where ions with larger critical energies exhibited higher survival yields. Survival yields for all native and all but the 4 M derivatized LISMA substrates remained unchanged as the fluence was increased. The survival yield of the 4 M ion on PFP-derivatized surface was constant up to 36 mJ/cm² and slightly declined above that.

To compare the energy transfer in ion production from LISMA with other ionization methods, the survival yields for 4 M ions desorbed from PFP-derivatized DIOS and from α -cyano-4-hydroxycinnamic acid (CHCA), a MALDI matrix,³⁹ were plotted along with our findings in Figure 3A. The threshold laser fluence required to desorb the TI from LISMA at 26 mJ/cm² is slightly higher than that of DIOS and MALDI (~24 mJ/cm²). Above the threshold, the preformed TI released by MALDI showed a sharp decline in survival yield that was in contrast with the steady behavior of TI desorbed from LISMA (see Figure 3A). This could be interpreted as an increase in internal

energy for the MALDI process, compared to an unchanged internal energy for LISMA desorbed ions as the laser fluence increased.

These results indicate that LISMA exhibits internal energy transfer similar to DIOS but with somewhat higher survival yields. Xiao et al. recently reported fluence dependent survival yields for TI desorbed in DIOS experiments.³⁷ They explained this discrepancy by the more than 2 orders of magnitude higher background pressure in their vacuum system compared to ours. Background pressure and surface adsorbates are known to have a strong influence on ion yields and fragmentation in laser desorption from silicon surfaces.⁴⁹

Our findings on the fluence dependence of peptide mass spectra produced by MALDI and LISMA seem to contradict our observations with TI. While MALDI time-of-flight mass spectra of peptides show little or no fragmentation, the mass spectra of bradykinin and other small peptides in LISMA experiments indicate declining survival yields as the fluence is raised. In other words, although increasing the laser fluence does not seem to affect the internal energy of the TI desorbed from LISMA, it does promote the fragmentation of peptides. The inset in Figure 2 demonstrates rapid decline for the survival yield of bradykinin with increasing fluence. The observations for these two molecular classes cannot be reconciled if the peptide fragmentation is solely attributed to the unimolecular decomposition of excited ions.

A possible explanation for this apparent contradiction is the presence of an alternative fragmentation pathway. In an earlier study based on the fragmentation pattern of the P₁₄R synthetic peptide, we hypothesized that the in-source fragmentation on LISMA substrates was induced by hydrogen radicals produced via the recombination of photoelectrons emitted from the silicon and protons generated from the residual solvent.³ According to the hypothesis, similar to a mechanism advanced for ECD, the hydrogen radicals attacked the peptide backbone and induced several pathways of fragmentation. These reactive fragmentation channels did not require the elevated internal energies necessary for the commonly utilized CAD. Comparing the ECD spectra for bradykinin and the other peptides in this study to the fragments produced by LISMA, however, brings this mechanism into question. As it is seen in Table 1, ECD spectra are rich in c- and z-series ions, whereas LISMA spectra are dominated by

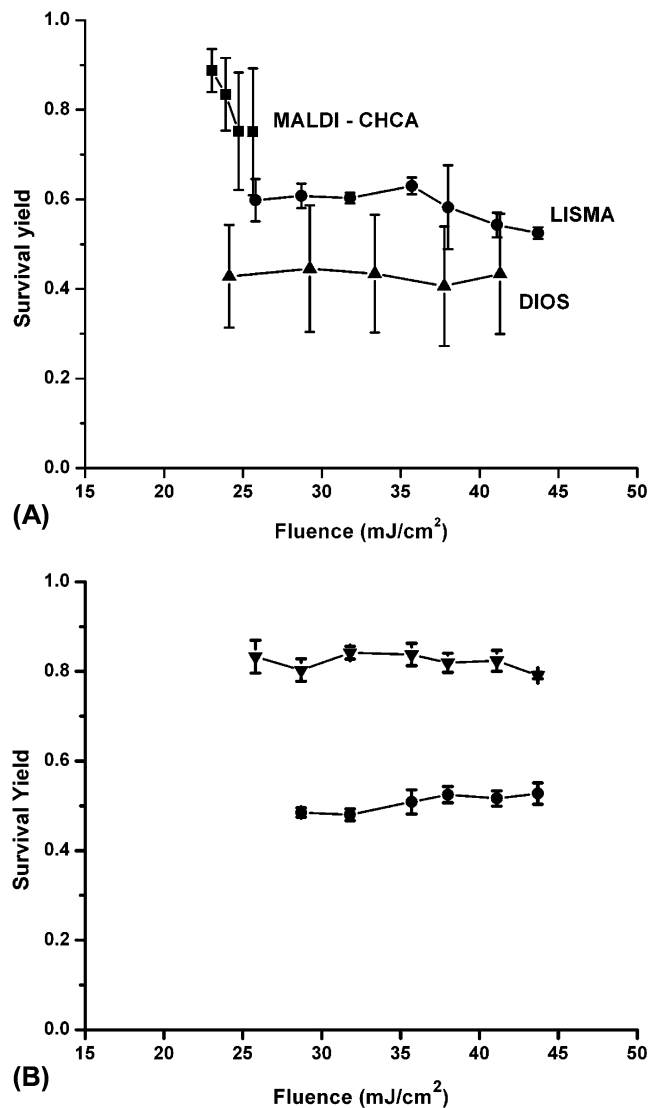


Figure 3. (A) Fluence dependence of 4 M benzylpyridinium TI survival yields drop precipitously in the case of MALDI from CHCA matrix⁶ (■), but remain mostly unchanged for desorption from PFP-derivatized LISMA (●) and PFP-derivatized DIOS¹¹ (▲). (B) The flat survival yield curve for 4F benzylpyridinium ions from native LISMA surfaces (●) is shifted to higher values for PFP-derivatized LISMA (▼).

a- and *y*-series ions. Alternative explanations can be based on the combination of free radical and CAD or SID-type channels as well as the field enhancement effects around the microcolumns and the differences between the transient dipole moments of the peptides and the TI.

Surface Derivatization. By altering the surface chemistry of LISMA through silylation, less polar and more hydrophobic surfaces were produced, which resulted in higher ion yields compared to native LISMA. As can be seen for the 4F benzylpyridinium ion in Figure 3B, in addition to enhanced ion production, derivatized LISMA surfaces also increased the survival yield. During the interaction of the LISMA with the laser radiation, the microcolumns heat up and impart some of their energy to the adsorbates.⁴ This energy transfer is modulated by the adsorbate–surface interaction. Native LISMA have terminal hydride and silanol groups that delay the release of polar adsorbates resulting in an increased energy transfer. The suppression of energy transfer to the TI on silylated LISMA is the consequence of reduced interaction energy between the adsorbate and the microcolumns.

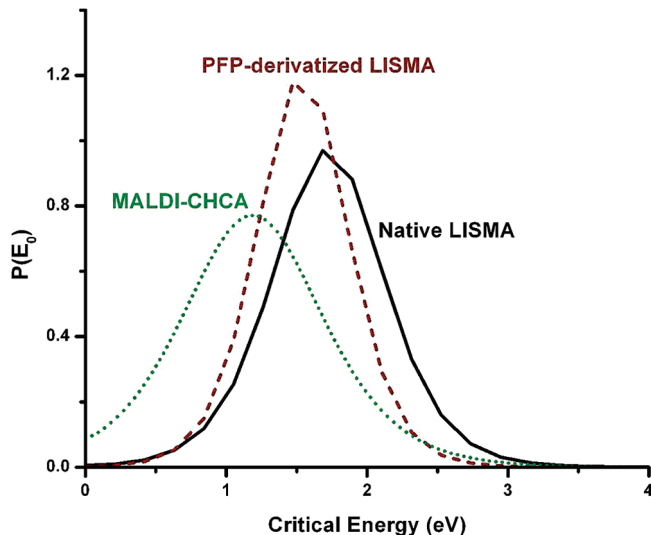


Figure 4. Internal energy distributions of TI desorbed from native LISMA (solid line in black) and PFP-derivatized LISMA (dashed line in wine color) at a laser fluence of 36 mJ/cm² and MALDI from CHCA matrix at a laser fluence of 26 mJ/cm² (dotted line in olive color, data adopted from ref 39).

The 4F benzylpyridinium ion exhibits the most pronounced survival yield difference between desorption from the native and the PFP-derivatized surfaces. The sharp reduction in energy transfer to the 4F ion is likely related to the weak fluorine–fluorine interactions with the PFP-derivatized layer compared to the strong affinity to the terminal hydride or silanol groups on native LISMA. Of the studied TI, the 4F ion is also the least polarizable leading to weaker ion surface interactions. This translates into the faster release of these ions and reduced energy transfer.

Internal Energies. Internal energy values for the TI were derived from the survival yield data using the RRKM theory. The internal energies of the TI desorbed from native LISMA were obtained by comparing the experimental rate coefficients of decomposition determined through eq 3 with the RRKM curves expressed by eq 4. Except for the 4Cl case, the derived internal energy values, $E_{\text{int}}(4\text{MO}) = 3.97$ eV, $E_{\text{int}}(4\text{M}) = 4.85$ eV, $E_{\text{int}}(2\text{M}) = 4.91$ eV, $E_{\text{int}}(3\text{M}) = 4.91$ eV, $E_{\text{int}}(3\text{MO}) = 8.18$ eV, $E_{\text{int}}(4\text{Cl}) = 4.48$ eV, and $E_{\text{int}}(4\text{F}) = 8.33$ eV, correlated well with the critical energies for their fragmentation. The internal energies determined as a function of laser fluence in the 26–44 mJ/cm² range remained essentially unchanged.

When compared with MALDI from CHCA, 3,5-dimethoxy-4-hydroxycinnamic acid (sinapinic acid) and 2,5-dihydroxybenzoic acid matrixes, TI desorbed from LISMA generally exhibited higher internal energies. In the MALDI experiments, the internal energies were dependent on the laser fluence.

As the eight TI exhibited a range of critical energies (from 1.3 to 2.2 eV), with the survival yield method we were able to extract the internal energy distributions at a particular laser fluence. The results are shown in Figure 4 for native (solid line) and derivatized (dashed line) LISMA with no corrections for the kinetic shift. At a laser fluence of 36 mJ/cm², the mean of the internal energy distribution in Figure 4 was slightly higher for native LISMA than for silane derivatized LISMA, with values of 1.73 and 1.59 eV respectively. The 0.14 eV lower internal energy on the derivatized surface corresponded to a significant increase in the survival yield. For comparison, the internal energy distribution of MALDI from CHCA matrix at a laser fluence of 26 mJ/cm² is also shown.³⁹ The mean internal energy distribution, 1.18 eV, was lower than derivatized and

native LISMA, as expected from the increased survival yield values shown in Figure 3A. In addition, the internal energy distribution from CHCA is broader than from LISMA, which may indicate a more dense plume.

The internal energies and their distributions for TI desorbed from native and derivatized LISMA structures indicated that the ion activation mechanism operational for peptides did not work for these benzylpyridinium ions. As the internal energy of TI did not change with increasing fluence, the declining survival yield of peptide ions at elevated laser fluences probably did not stem from an increase in their internal energy induced by the desorption process.

Conclusions

Due to their role in the structural studies of biomolecules, new ionization methods are vigorously investigated. Mesos-structured surfaces, such as LISMA, are the basis of emerging techniques for the laser desorption ionization of a broad class of molecules. LISMA is the first ionization platform to exhibit nanophotonic ion production for mass spectrometry. In contrast to most conventional methods, laser desorption ionization of peptides from LISMA induces adjustable structure-specific fragmentation without additional ion activation techniques. From the high-fluence mass spectra it is clear that the related processes take place in the ion source of the mass spectrometer (in-source decay). Thus, the half-life time of the activated species must be comparable to the residence time of the ions in the ion source region (<100 ns).

Model peptides desorbed from LISMA showed fluence dependent fragmentation. At low laser fluences, mostly quasi-molecular ions were observed. As the fluence was raised, the abundance and variety of structure specific peptide fragments increased. The resulting fragment ions were compared to the dissociation products, and related energetics, formed in other methods of ionization, such as low- and high-energy CAD, BIRD, ECD, SID, and interactions with metastable helium atoms. Surveying the fragment ions produced by LISMA, we discovered that both low- and high-energy channels were active. Similarities in the high-fluence LISMA mass spectra of small peptides (bradykinin, leucine enkephalin, etc.) to conventional SID spectra indicated that a similar activation mechanism, i.e., ion collisions with the microcolumn surfaces, might play a role in ion activation.

To discern if the internal energy of the ion gained in the desorption step plays a role in the fragmentation, the survival yields of TI were analyzed. We found that the internal energy transfer from LISMA and thus the degree of TI fragmentation were independent of the applied laser fluence. Furthermore, silane-derivatization of LISMA decreased the surface-adsorbate interaction and resulted in higher survival yields. These results for TI are in conflict with the strong fluence dependence of the survival yield for peptides.

Earlier studies indicated that nanophotonic structures, such as LISMA, enable new ways to couple laser energy into the desorption and ionization process. In this contribution, we showed that the interaction of laser radiation with LISMA also provides a novel way for peptide ion activation. This method accessed both low- and high-energy fragmentation channels.

The mechanism of ion activation remains unresolved. Likely factors in this process include the enhancement of the electromagnetic field near the microcolumns, surface activation due to ion-surface collisions, and reactive channels, including hydrogen radical attack on the peptide backbone. At this point none of these mechanisms provides an explanation for all of

the experimental findings in this study. For example, if surface activation plays a role in the peptide fragmentation why does the survival yield of the TI stay unchanged in a broad fluence range? To explain the presence of low- and high-energy fragments in the peptide spectra, one might have to consider the combined effect of several mechanisms.

To gain further insight into the role of these effects in ionization, nanofabricated structures with tailored column diameter, height, and periodicity can be produced. For example, by changing the aspect ratio of the columns to 10:1, the local field enhancement can be increased to $\kappa \approx 13$ and correspondingly the near-field laser irradiance is raised by a factor of ~ 169 . Thus, following the peptide fragmentation with changing column aspect ratio can indicate the significance of near-field effects. Increasing the periodicity enlarges the trough width and reduces the contribution of surface collisions. Lowering the delay time in delayed extraction experiments results in shorter residence time in the ion source that, in turn, limits the impact of reactive fragmentation channels. In addition to the residual solvents that are always present on these surfaces, other reactants can be introduced into the structures to promote ionization and/or fragmentation through reactions.

Due to the features of LISMA discussed in this paper, their potential applications include the preparation of diverse ionic species. The ability of this nanostructure to induce peptide fragmentation without the use of CAD, ECD, or other activation method, presents a simple approach to structural elucidation in chemical analysis.

Acknowledgment. The authors are thankful for the financial support from the Chemical Sciences, Geosciences and Biosciences Division, Office of Basic Energy Sciences, Office of Science, U.S. Department of Energy (DE-FG02-01ER15129) and from Protea Biosciences Inc. Support from the Department of Energy does not constitute an endorsement of the views expressed in the article. The MassKinetics Scientific program provided by K. Vekey and L. Drahos of the Institute of Chemistry at the Chemical Research Center of the Hungarian Academy of Sciences enabled the straightforward calculation of RRKM rate coefficients. This help is greatly appreciated.

References and Notes

- (1) Her, T. H.; Finlay, R. J.; Wu, C.; Deliwala, S.; Mazur, E. *Appl. Phys. Lett.* **1998**, *73*, 1673–1675.
- (2) Pedraza, A. J.; Fowlkes, J. D.; Lowndes, D. H. *Appl. Phys. Lett.* **1999**, *74*, 2322–2324.
- (3) Chen, Y.; Vertes, A. *Anal. Chem.* **2006**, *78*, 5835–5844.
- (4) Walker, B. N.; Razunguzwa, T.; Powell, M.; Knochenmuss, R.; Vertes, A. *Angew. Chem., Int. Ed.* **2009**, *48*, 1669–1672.
- (5) Hamann, H. F.; Gallagher, A.; Nesbitt, D. J. *Appl. Phys. Lett.* **2000**, *76*, 1953–1955.
- (6) Luo, G. H.; Marginean, I.; Vertes, A. *Anal. Chem.* **2002**, *74*, 6185–6190.
- (7) Gabelica, V.; Schulz, E.; Karas, M. *J. Mass Spectrom.* **2004**, *39*, 579–593.
- (8) Campbell, J. M.; Vestal, M. L.; Blank, P. S.; Stein, S. E.; Epstein, J. A.; Yergey, A. L. *J. Am. Soc. Mass Spectrom.* **2007**, *18*, 607–616.
- (9) Wei, J.; Buriak, J. M.; Siuzdak, G. *Nature* **1999**, *399*, 243–246.
- (10) Northen, T. R.; Yanes, O.; Northen, M. T.; Marrinucci, D.; Uritboonthai, W.; Apon, J.; Golledge, S. L.; Nordstrom, A.; Siuzdak, G. *Nature* **2007**, *449*, 1033–1033.
- (11) Luo, G. H.; Chen, Y.; Siuzdak, G.; Vertes, A. *J. Phys. Chem. B* **2005**, *109*, 24450–24456.
- (12) Butcher, D. J.; Asano, K. G.; Goeringer, D. E.; McLuckey, S. A. *J. Phys. Chem. A* **1999**, *103*, 8664–8671.
- (13) Vachet, R. W.; Winders, A. D.; Glish, G. L. *Anal. Chem.* **1996**, *68*, 522–526.
- (14) Schnier, P. D.; Price, W. D.; Jockusch, R. A.; Williams, E. R. *J. Am. Chem. Soc.* **1996**, *118*, 7178–7189.
- (15) McCormack, A. L.; Somogyi, A.; Dongre, A. R.; Wysocki, V. H. *Anal. Chem.* **1993**, *65*, 2859–2872.

- (16) Laskin, J. *J. Phys. Chem. A* **2006**, *110*, 8554–8562.
- (17) Despeyroux, D.; Wright, A. D.; Jennings, K. R. *Int. J. Mass Spectrom. Ion Processes* **1993**, *126*, 95–99.
- (18) Gorshkov, M. V.; Masselon, C. D.; Nikolaev, E. N.; Udseth, H. R.; Pasa-Tolic, L.; Smith, R. D. *Int. J. Mass Spectrom.* **2004**, *234*, 131–136.
- (19) Polfer, N. C.; Haselmann, K. F.; Langridge-Smith, P. R. R.; Barran, P. E. *Mol. Phys.* **2005**, *103*, 1481–1489.
- (20) Syka, J. E. P.; Coon, J. J.; Schroeder, M. J.; Shabanowitz, J.; Hunt, D. F. *Proc. Natl. Acad. Sci. U.S.A.* **2004**, *101*, 9528–9533.
- (21) Berkout, V. D. *Anal. Chem.* **2006**, *78*, 3055–3061.
- (22) Berkout, V. D.; Doroshenko, V. M. *Int. J. Mass Spectrom.* **2008**, *278*, 150–157.
- (23) Berkout, V. D. *Anal. Chem.* **2009**, *81*, 725–731.
- (24) Derwa, F.; Depauw, E.; Natalis, P. *Org. Mass Spectrom.* **1991**, *26*, 117–118.
- (25) Vekey, K. *J. Mass Spectrom.* **1996**, *31*, 445–463.
- (26) Collette, C.; Drahos, L.; De Pauw, E.; Vekey, K. *Rapid Commun. Mass Spectrom.* **1998**, *12*, 1673–1678.
- (27) Collette, C.; De Pauw, E. *Rapid Commun. Mass Spectrom.* **1998**, *12*, 165–170.
- (28) Drahos, L.; Heeren, R. M. A.; Collette, C.; De Pauw, E.; Vekey, K. *J. Mass Spectrom.* **1999**, *34*, 1373–1379.
- (29) Gabelica, V.; De Pauw, E. *Mass Spectrom. Rev.* **2005**, *24*, 566–587.
- (30) Naban-Maillet, J.; Lesage, D.; Bossee, A.; Gimbert, Y.; Sztaray, J.; Vekey, K.; Tabet, J. C. *J. Mass Spectrom.* **2005**, *40*, 1–8.
- (31) Pak, A.; Lesage, D.; Gimbert, Y.; Vekey, K.; Tabet, J. C. *J. Mass Spectrom.* **2008**, *43*, 447–455.
- (32) Gabelica, V.; De Pauw, E.; Karas, M. *Int. J. Mass Spectrom.* **2004**, *231*, 189–195.
- (33) Greisch, J. F.; Gabelica, V.; Remacle, F.; De Pauw, E. *Rapid Commun. Mass Spectrom.* **2003**, *17*, 1847–1854.
- (34) Vertes, A.; Luo, G. H.; Ye, L.; Chen, Y.; Marginean, I. *Appl. Phys. A: Mater. Sci. Process.* **2004**, *79*, 823–825.
- (35) Luo, G.; Marginean, I.; Ye, L.; Vertes, A. *J. Phys. Chem. B* **2008**, *112*, 6952–6956.
- (36) Stevenson, E.; Breuker, K.; Zenobi, R. *J. Mass Spectrom.* **2000**, *35*, 1035–1041.
- (37) Xiao, Y. S.; Retterer, S. T.; Thomas, D. K.; Tao, J. Y.; He, L. *J. Phys. Chem. C* **2009**, *113*, 3076–3083.
- (38) Nefliu, M.; Smith, J. N.; Venter, A.; Cooks, R. G. *J. Am. Soc. Mass Spectrom.* **2008**, *19*, 420–427.
- (39) Luo, G. H.; Chen, Y.; Daniels, H.; Dubrow, R.; Vertes, A. *J. Phys. Chem. B* **2006**, *110*, 13381–13386.
- (40) Vékely, K.; Brenton, A. G.; Beynon, J. H. *Int. J. Mass Spectrom. Ion Processes* **1986**, *70*, 277–300.
- (41) Kenttamaa, H. I.; Cooks, R. G. *Int. J. Mass Spectrom. Ion Processes* **1985**, *64*, 79–83.
- (42) Wysocki, V. H.; Kenttamaa, H. I.; Cooks, R. G. *Int. J. Mass Spectrom. Ion Processes* **1987**, *75*, 181–208.
- (43) Williams, D. H.; Naylor, S. *J. Chem. Soc., Chem. Commun.* **1987**, 1408–1409.
- (44) Frankevich, V.; Knochenmuss, R.; Zenobi, R. *Int. J. Mass Spectrom.* **2002**, *220*, 11–19.
- (45) Afanas'ev, V. V.; Stesmans, A. *Europhys. Lett.* **2001**, *53*, 233–239.
- (46) Chen, Y.; Vertes, A. *J. Phys. Chem. A* **2003**, *107*, 9754–9761.
- (47) Baer, T.; Mayer, P. M. *J. Am. Soc. Mass Spectrom.* **1997**, *8*, 103–115.
- (48) Drahos, L.; Vekey, K. *J. Mass Spectrom.* **2001**, *36*, 237–263.
- (49) Chen, Y. F.; Chen, H. Y.; Aleksandrov, A.; Orlando, T. M. *J. Phys. Chem. C* **2008**, *112*, 6953–6960.

JP906834Z